Electronic Supplementary Material (ESI) for Materials Chemistry Frontiers.

Upconversion and multiexciton generation in organic Mn(II) complex boost quantum yield > 100%

Atanu Jana,[a,b] *Chang Woo Myung,*[c] *Vijaya Gopalan Sree*[b] *and Kwang S. Kim**[a]

[a]Center for Superfunctional Materials, Department of Chemistry, Ulsan National Institute of Science and Technology (UNIST), 50 Unist-gil, Ulsan 44919, South Korea.

[b]Division of Physics and Semiconductor Science, Dongguk University, Seoul 04620, South Korea.

[c] Department of Chemistry, Chungnam National University, 99 Daehak-ro, Daejeon 34134, South Korea.

*E-mail: *kimks@unist.ac.kr*

Characterizations

The powder X-ray diffraction (PXRD) was performed on D/MAX2500V/PC diffractometer, Rigaku using Cu-rotating anode x-ray. X-ray photoelectron spectra (XPS) were collected using K-alpha model, ThermoFisher. During the measurement, the Bragg's diffraction angle (2θ) range was set to 10-50° and scan rate was 2°/ minute. The sample was absolutely pure with no apparent impurity or precursors present in the resolution limit of X-ray diffraction analysis.

Scanning electron microscopy (SEM) images were taken using SU8220 Cold FE-SEM, Hitach High-Technologies.

Thermogravimetric analysis (TGA) has been carried out using Q500 model, TA.

The optical diffuse reflectance spectra of all solid samples were collected using a Cary 5000 UV-Vis-NIR Spectrophotometer, (Agilent) with integrated sphere in diffuse-reflectance mode and then converted to Kubelka-Munk function, F(R).

All the photoluminescence (PL) spectra was collected using Cary Eclipse fluorometer, (Varian) in solid state.

Photoluminescence quantum yield (PLQY) has been experimentally evaluated using FP-8500ST Spectrofluorometer, (Jasco International). PLQY has been evaluated by integrating sphere and the following equations have been used:

Quantum yield [%] = $S_2/(S_0-S_1) \times 100$

S_1 = area scattered from the sample, S_2 = area emitted from sample, S_0 = area from incident light. S_0 was measured with nothing in the sample holder.

Time-resolved photoluminescence spectrum was collected using NF900 (FLS920), (Edinburgh Instrument, UK). The time-resolved photoluminescence spectrum was fitted by tail-fit model according to the equation: [1] $I\ (t) = \sum_{i=1}^{\pi} A_i e^{-\frac{t}{\tau_i}}$

$A_i =$ Amplitude of the i^{th} component, in counts, in the first fitting range channel,

t_i = Lifetime of the i^{th} component

Single crystal X-ray diffraction measurements.

Single crystal X-ray diffraction analysis was performed at Wester Seoul center of KBSI. A green crystal was picked up with paraton oil and mounted on a Bruker D8 Venture PHOTON 100 CMOS diffractometer equipped with graphite-monochromated Mo Kα (λ= 0.7107Å) radiation source at 25 ℃. The goniometer equipped with the diffractometer is KAPPA four circle goniometer with φ, κ, ω and 2θ axes by which the crystal is rotated. The unit cell parameters were evaluated by collecting the diffracted intensities from 24 frames measured in two different crystallographic zones and using the method of difference vectors. Data collection and integration were carried out with SMART APEX2 (Bruker, 2012) and SAINT (Bruker, 2012). Absorption correction was done by multi-scan method implemented in SADABS. The crystal structure was solved by direct methods and refined by full-matrix least-squares on F^2

using SHELXTL. All the non-hydrogen atoms were refined anisotropically, and hydrogen atoms were added to their geometrically ideal positions.

Density functional theory and many-body calculations. We used Vienna Ab initio Simulation Package (VASP)[2] for spin-polarized DFT calculations using PBE functional plus Tkatchenko-Scheffler (TS) van der Waals correction,[3] scissor correction and BSE calculation. We used (6×6×4), (4×2×2) and (2×2×1) k-point meshes for $MnBr_2$, Me_3NPhBr and $[Me_3NPh]_2MnBr_4$, respectively with 500 eV energy cutoff. Due to overestimation of the band gap on Mn compounds and computational load of GW0 calculations which requires a large number of unoccupied bands, we used scissor correction $\Delta_{sc}(MnBr_2)$ = 0.27 eV and $\Delta_{sc}(Me_3NPhBr)$ = 1.14 eV. We employed 20 % of the exact Hartree-Fock (HF) exchange instead of using the exchange interactions calculated from GW0 to solve BSE equations. This is more feasible and consistent for the calculation of compound **1** that contains 636 atoms and 1836 electrons in the crystal unit cell along with its precursors. Also to be consistent, we found the optimal HF exchange rate for the exciton binding energy of sc+BSE that is comparable to GW0+BSE.

Device fabrication and measurement.

The HIL, poly(3,4-ethylenedioxythiophene):polystyrenesulfonate (PEDOT:PSS) was spin coated onto the UV-Ozone treated ITO-coated glass substrate, followed by annealing in air for 15 min at 150 ^oC, respectively. The hole transporting layers (HTL) and EML (Solvent: CH_2Cl_2 1 wt%) was then spin-coated onto the HIL inside the glove box in nitrogen atmosphere. ETL, LiF and Al were sequentially deposited over the EML layer in vacuum at a pressure of 5×10^{-6} Torr. All measurements of devices were carried out under ambient condition at RT. Device architecture of the devices are:

Device 1A: ITO/PEDOT:PSS (30 nm)/TAPC (20 nm)/mCP (10 nm)/mCP:TPBi(dopant **(1)** 5 wt%)/TmPyPB (40 nm)/LiF (1 nm)/Al (120 nm).

Device 1B: ITO/PEDOT:PSS (30 nm)/TAPC (20 nm)/mCP (10 nm)/mCP:TPBi(dopant **(1)** 10 wt%)/TmPyPB (40 nm)/LiF (1 nm)/Al (120 nm).

Device 1C: ITO/PEDOT:PSS (30 nm)/TAPC (20 nm)/mCP (10 nm)/mCP:TPBi(dopant **(1)** 13 wt%)/TmPyPB (40 nm)/LiF (1 nm)/Al (120 nm).

Device 1D: ITO/PEDOT:PSS (30 nm)/TAPC (20 nm)/mCP (10 nm)/mCP:TPBi(dopant **(1)** 15 wt%)/TmPyPB (40 nm)/LiF (1 nm)/Al (120 nm).

Device 1E: ITO/PEDOT:PSS (30 nm)/TAPC (20 nm)/mCP (10 nm)/mCP:TPBi(dopant **(1)** 20 wt%)/TmPyPB (40 nm)/LiF (1 nm)/Al (120 nm).

Device 2: ITO/PEDOT:PSS (30 nm)/TAPC (20 nm)/mCP (10 nm)/CBP:TPBi(dopant **(1)** 13 wt%)/ TmPyPB (40 nm)/LiF (1 nm)/Al (120 nm).

Device 3: ITO/PEDOT:PSS (30 nm)/TAPC (20 nm)/TAPC:TPBi(dopant **(1)** 13 wt%)/ TmPyPB (40 nm)/LiF (1 nm)/Al (120 nm).

The current density and voltage were controlled with a measurement unit (Keithley, model 236) power source. The luminance, current efficiency, power efficiency, external quantum efficiency (EQE), CIE coordinates (x, y), current density characteristics, and EL spectra were measured by a spectra scan CS-2000 photometer (Minolta).

Tables

Table S1. Crystal data and structure refinement for Me_3NPhBr.		
Identification code	Me_3NPhBr	
Empirical formula	C9 H14 Br N	
Formula weight	216.12	
Temperature	293(2) K	
Wavelength	0.71073 Å	
Crystal system	Orthorhombic	
Space group	$P2_12_12_1$	
Unit cell dimensions	a = 6.8492(4) Å	α= 90°.
	b = 10.7579(7) Å	β= 90°.
	c = 13.7900(8) Å	γ= 90°.
Volume	1016.09(11) $Å^3$	
Z	4	
Density (calculated)	1.413 Mg/m^3	
Absorption coefficient	3.989 mm^{-1}	
F(000)	440	
Crystal size	0.210 x 0.150 x 0.110 mm^3	
Theta range for data collection	2.401 to 28.325°.	
Index ranges	-8<=h<=9, -14<=k<=14, -18<=l<=18	
Reflections collected	29778	
Independent reflections	2522 [R(int) = 0.0432]	
Completeness to theta = 25.242°	100.0 %	
Absorption correction	Semi-empirical from equivalents	
Max. and min. transmission	0.7457 and 0.5090	
Refinement method	Full-matrix least-squares on F^2	
Data / restraints / parameters	2522 / 0 / 103	
Goodness-of-fit on F^2	1.076	
Final R indices [I>2sigma(I)]	R1 = 0.0225, wR2 = 0.0524	
R indices (all data)	R1 = 0.0300, wR2 = 0.0566	
Absolute structure parameter	0.000(5)	
Extinction coefficient	n/a	
Largest diff. peak and hole	0.401 and -0.169 e.$Å^{-3}$	

Table S2. Structural parameters of Me_3NPhBr.

Bond lengths [Å]		Bond angles [°]	
N(1)-C(4)	1.499(4)		
N(1)-C(1)	1.505(4)	C(4)-N(1)-C(1)	108.1(2)
N(1)-C(2)	1.507(4)	C(4)-N(1)-C(2)	111.3(2)
N(1)-C(3)	1.508(4)	C(1)-N(1)-C(2)	110.0(2)
C(1)-H(1A)	0.9600	C(4)-N(1)-C(3)	113.0(2)
C(1)-H(1B)	0.9600	C(1)-N(1)-C(3)	107.4(2)
C(1)-H(1C)	0.9600	C(2)-N(1)-C(3)	107.0(2)
C(2)-H(2A)	0.9600	N(1)-C(1)-H(1A)	109.5
C(2)-H(2B)	0.9600	N(1)-C(1)-H(1B)	109.5
C(2)-H(2C)	0.9600	H(1A)-C(1)-H(1B)	109.5
C(3)-H(3A)	0.9600	N(1)-C(1)-H(1C)	109.5
C(3)-H(3B)	0.9600	H(1A)-C(1)-H(1C)	109.5
C(3)-H(3C)	0.9600	H(1B)-C(1)-H(1C)	109.5
C(4)-C(9)	1.377(4)	N(1)-C(2)-H(2A)	109.5
C(4)-C(5)	1.380(4)	N(1)-C(2)-H(2B)	109.5
C(5)-C(6)	1.383(4)	H(2A)-C(2)-H(2B)	109.5
C(5)-H(5)	0.9300	N(1)-C(2)-H(2C)	109.5
C(6)-C(7)	1.376(5)	H(2A)-C(2)-H(2C)	109.5
C(6)-H(6)	0.9300	H(2B)-C(2)-H(2C)	109.5
C(7)-C(8)	1.370(5)	N(1)-C(3)-H(3A)	109.5
C(7)-H(7)	0.9300	N(1)-C(3)-H(3B)	109.5
C(8)-C(9)	1.381(5)	H(3A)-C(3)-H(3B)	109.5
C(8)-H(8)	0.9300	N(1)-C(3)-H(3C)	109.5
C(9)-H(9)	0.9300	H(3A)-C(3)-H(3C)	109.5
		H(3B)-C(3)-H(3C)	109.5
		C(9)-C(4)-C(5)	120.3(3)
		C(9)-C(4)-N(1)	122.0(3)
		C(5)-C(4)-N(1)	117.7(3)
		C(4)-C(5)-C(6)	119.6(3)
		C(4)-C(5)-H(5)	120.2
		C(6)-C(5)-H(5)	120.2
		C(7)-C(6)-C(5)	120.2(3)

Table S3. Crystal data and structure refinement for $[Me_3NPh]_2MnBr_4$ (**1**).		
Identification code	$[Me_3NPh]_2MnBr_4$	
Empirical formula	C18H28Br4MnN2	
Formula weight	647.00	
Temperature	293(2) K	
Wavelength	0.71073 Å	
Crystal system	Monoclinic	
Space group	C2/c	
Unit cell dimensions	a = 17.1271(9) Å	α = 90°.
	b = 9.1787(5) Å	β = 92.605(2)°.
	c = 47.166(3) Å	γ = 90°.
Volume	7407.1(7) $Å^3$	
Z	12	
Density (calculated)	1.741 Mg/m^3	
Absorption coefficient	7.012 mm^{-1}	
F(000)	3780	
Crystal size	0.220 x 0.150 x 0.120 mm^3	
Theta range for data collection	2.381 to 28.380°.	
Index ranges	-22<=h<=22, -12<=k<=12, -62<=l<=62	
Reflections collected	116783	
Independent reflections	9231 [R(int) = 0.0673]	
Completeness to theta = 25.242°	100.0 %	
Absorption correction	Semi-empirical from equivalents	
Max. and min. transmission	0.7457 and 0.5415	
Refinement method	Full-matrix least-squares on F^2	
Data / restraints / parameters	9231 / 6 / 348	
Goodness-of-fit on F^2	1.077	
Final R indices [I>2sigma(I)]	R1 = 0.0438, wR2 = 0.0833	
R indices (all data)	R1 = 0.0789, wR2 = 0.0937	
Extinction coefficient	n/a	
Largest diff. peak and hole	0.753 and -0.481 e.$Å^{-3}$	

Table S4. Structural parameters of $[Me_3NPh]_2MnBr_4$ (**1**).

Bond lengths [Å]		Bond angles [°]	
Mn(1)-Br(2)	2.4979(6)	Br(2)-Mn(1)-Br(2)#1	107.75(4)
Mn(1)-Br(2)#1	2.4980(6)	Br(2)-Mn(1)-Br(1)#1	109.053(16)
Mn(1)-Br(1)#1	2.5086(6)	Br(2)#1-Mn(1)-Br(1)#1	113.911(16)
Mn(1)-Br(1)	2.5087(6)	Br(2)-Mn(1)-Br(1)	113.910(16)
Mn(2)-Br(6)	2.4928(8)	Br(2)#1-Mn(1)-Br(1)	109.049(16)
Mn(2)-Br(4)	2.4946(7)	Br(1)#1-Mn(1)-Br(1)	103.28(3)
Mn(2)-Br(5)	2.4982(8)	Br(6)-Mn(2)-Br(4)	109.32(3)
Mn(2)-Br(3)	2.4984(8)	Br(6)-Mn(2)-Br(5)	107.81(3)
N(1)-C(3)	1.443(10)	Br(4)-Mn(2)-Br(5)	107.34(3)
N(1)-C(1)	1.468(7)	Br(6)-Mn(2)-Br(3)	110.29(3)
N(1)-C(2)	1.484(9)	Br(4)-Mn(2)-Br(3)	108.47(3)
N(1)-C(4)	1.488(6)	Br(5)-Mn(2)-Br(3)	113.51(3)
C(1)-H(1A)	0.9600	C(3)-N(1)-C(1)	107.9(6)
C(1)-H(1B)	0.9600	C(3)-N(1)-C(2)	106.9(6)
C(1)-H(1C)	0.9600	C(1)-N(1)-C(2)	106.9(6)
C(2)-H(2A)	0.9600	C(3)-N(1)-C(4)	111.9(6)
C(2)-H(2B)	0.9600	C(1)-N(1)-C(4)	112.8(4)
C(2)-H(2C)	0.9600	C(2)-N(1)-C(4)	110.1(4)
C(3)-H(3A)	0.9600	N(1)-C(1)-H(1A)	109.5
C(3)-H(3B)	0.9600	N(1)-C(1)-H(1B)	109.5
C(3)-H(3C)	0.9600	H(1A)-C(1)-H(1B)	109.5
C(4)-C(5)	1.357(6)	N(1)-C(1)-H(1C)	109.5
C(4)-C(9)	1.360(7)	H(1A)-C(1)-H(1C)	109.5
C(5)-C(6)	1.356(8)	H(1B)-C(1)-H(1C)	109.5
C(5)-H(5)	0.9300	N(1)-C(2)-H(2A)	109.5
C(6)-C(7)	1.340(8)	N(1)-C(2)-H(2B)	109.5
C(6)-H(6)	0.9300	H(2A)-C(2)-H(2B)	109.5
C(7)-C(8)	1.333(8)	N(1)-C(2)-H(2C)	109.5
C(7)-H(7)	0.9300	H(2A)-C(2)-H(2C)	109.5
C(8)-C(9)	1.364(7)	H(2B)-C(2)-H(2C)	109.5
C(8)-H(8)	0.9300	N(1)-C(3)-H(3A)	109.5
C(9)-H(9)	0.9300		
N(2)-C(10)	1.484(5)		
N(2)-C(13)	1.502(5)		
N(2)-C(12)	1.503(5)		
N(2)-C(11)	1.506(5)		
C(10)-H(10A)	0.9600		
C(10)-H(10B)	0.9600		
C(10)-H(10C)	0.9600		
C(11)-H(11A)	0.9600		
C(11)-H(11B)	0.9600		
C(11)-H(11C)	0.9600		

C(12)-H(12A)	0.9600	
C(12)-H(12B)	0.9600	
C(12)-H(12C)	0.9600	
C(13)-C(18)	1.363(6)	
C(13)-C(14)	1.371(6)	
C(14)-C(15)	1.373(7)	
C(14)-H(14)	0.9300	
C(15)-C(16)	1.350(9)	
C(15)-H(15)	0.9300	
C(16)-C(17)	1.355(9)	
C(16)-H(16)	0.9300	
C(17)-C(18)	1.381(7)	
C(17)-H(17)	0.9300	
C(18)-H(18)	0.9300	
N(3)-C(19)	1.487(6)	
N(3)-C(22)	1.500(5)	
N(3)-C(21)	1.504(5)	
N(3)-C(20)	1.515(5)	
C(19)-H(19A)	0.9600	

Table S5. Absorbance wavelengths and corresponding energies for excited states.

Wavelength (nm)	Frequency (cm^{-1})	Energy (eV)	Quartet states
472	21187	2.62	$^4T_1$ (^4G)
455	21978	2.72	$^4T_2$ (^4G)
436	22936	2.84	^4E, $^4A_1$ (^4G)
396	25253	3.13	$^4T_2$ (^4D)
370	27027	3.35	^4E (^4D)
361	27701	3.43	$^4T_1$ (^4P)
355	28169	3.49	-
309	32363	4.01	-
288	34723	4.30	-
277	36101	4.47	$^4A_2$ (^4F)
267	37453	4.64	$^4T_1$ (^4F)
260	38462	4.76	$^4T_2$ (^4F)
227	44053	5.46	-

Table S6. Excitation and emission wavelengths for below band gap energy excitations.

Excitation wavelength (nm)/ Energy (eV)	2×Energy of photons (eV)	Emission wavelength (nm)/ Energy (eV)
650/1.90	3.8	574/2.16, 597/2.07, 607/2.04
670/1.85	3.7	546/2.27, 573/2.16, 597/2.07, 604/2.05, 609/2.03
690/1.79	3.58	420/2.95, 546/2.27, 554/2.23, 574/2.16, 597/2.07, 607/2.04
710/1.74	3.48	441/2.81, 514/2.41, 547/2.26, 561/2.21, 570/2.17, 597/2.07, 605/2.04
730/1.69	3.38	462/2.68, 535/2.31
750/1.65	3.3	484/2.56, 555/2.23
770/1.61	3.22	464/2.67, 504/2.46, 573/2.16
790/1.56	3.12	486/2.55, 524/2.36, 595/2.08
8001.55	3.1	494/2.50, 534/2.32, 603/2.05
820/1.51	3.02	518/2.39, 556/2.22
840/1.47	2.94	537/2.30, 577/2.14
860/1.44	2.88	-
880/1.409	2.81	-

Table S7. PL QY of ionic Mn(II) single crystals

Serial	Compounds	Excitation wavelength (nm)	Emission wavelength (nm)	PL QY (%)	References
1	$[(benzothiazole\text{-}H)_2(MnBr_4)]\cdot 2H_2O$	468	530	26.18	[4]
2	$(diisopropylammonium)_2MnBr_4$	361	525	62	[5]
3	$[(BzMe_3N)]_2[MnBr_4]$	360	514	72.26	[6]
4	$[Ph_4P]_2[MnBr_4]$	-	516	98	[7]
5	[N-butyl-N-methylpyrrolidinium]$_2$[$MnBr_4$]	450	520	81	[8]
6	[N-butyl-N-methylpiperidinium]$_2$[$MnBr_4$]	450	527	55	[8]
7	[(1-buty-1-methylpyrrolidinium]$_2$[$MnBr_4$]	450	528	81.08	[9]
8	$[Et_4N]_2[MnBr_4]$	-	516	86	[10]
9	$[TMPEA]_2[MnBr_4]$	395	520	98	[11]
10	[ethylenebis-triphenylphosphonium]$_2$[$MnBr_4$]	-	517	95	[12]
11	[Allyltriphenylphosphonium]$_2$[$MnBr_4$]	450	516	48	[13]
12	$[Bu_4N]_2[MnBr_4]$	380	520	47	[14]
13	[Pyrrolidinium]$_2$[$MnBr_4$]	369	525	16.04	[15]
14	[Pyridinium]$_2$[$MnBr_4$]	460	521	95	[16]
15	$[Me_3NPh]_2MnBr_4$	227	521	188.79	Our current work
		236	521	123.95	
		250	521	94.57	
		280	521	71.57	
		300	521	49.95	
		350	521	25.61	
		365	521	69.69	
		377	521	68.00	
		390	521	62.67	
		455	521	67.49	
		472	521	66.07	

Figures

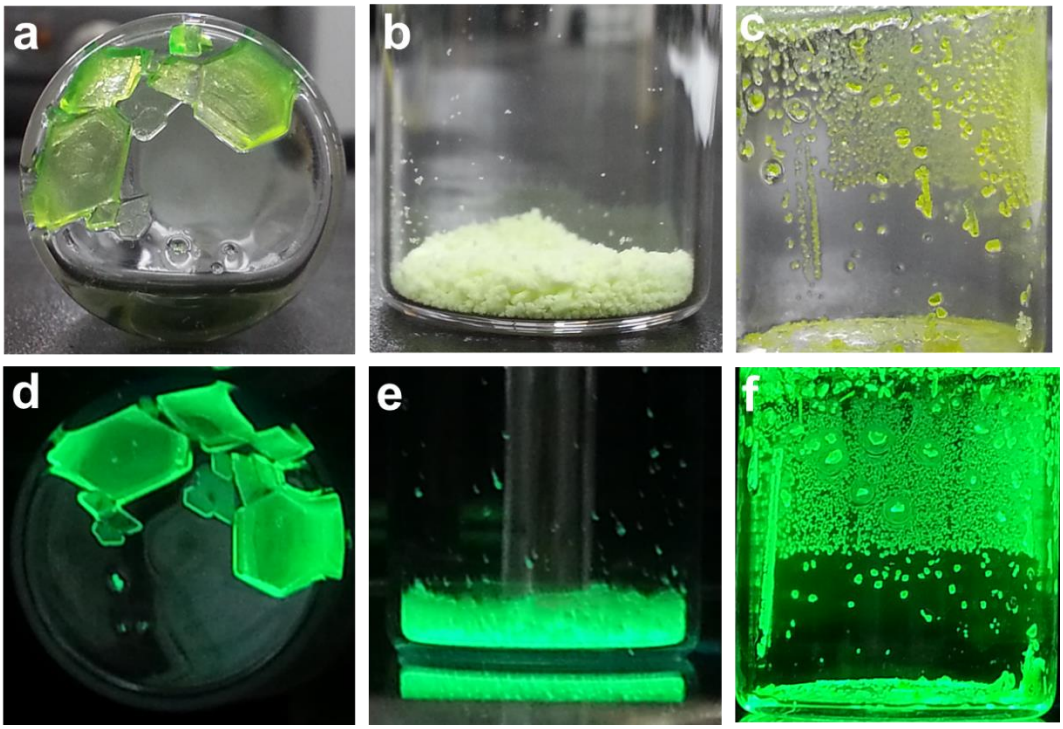

Figure S1. Crystal and powder form. **a,** Single crystal **(**SC) of $[Me_3NPh]_2MnBr_4$ (**1**). **b,** powder form of **1** synthesized by SIP method. **c**, Cs_4PbBr_6 (**2**) crystal under ambient light. **d,** SC of $[Me_3NPh]_2MnBr_4$ (**1**). **e,** powder form of **1** synthesized by SIP method. **f**, Cs_4PbBr_6 (**2**) crystal under ambient light.

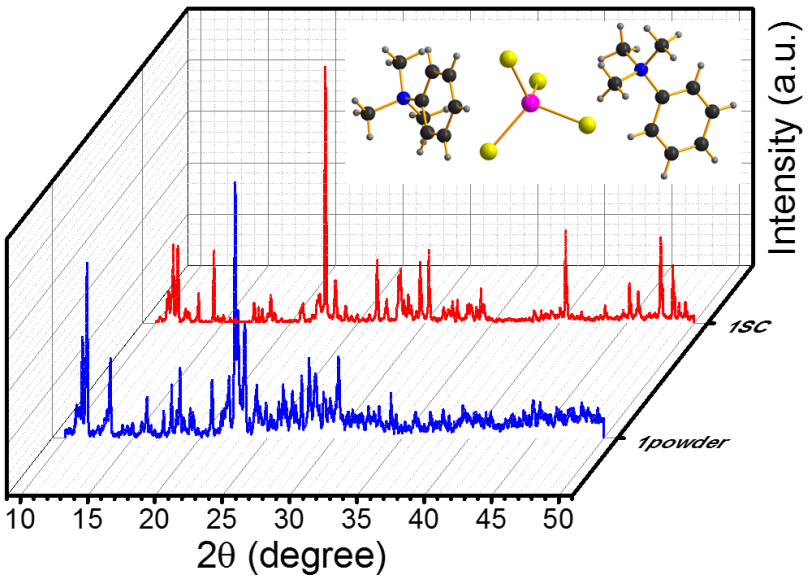

Figure S2. PXRD measurement. PXRD of (a) **1** and (b) Powder **1**. The well-matched PXRD patterns of SC and powder form indicate their similar crystal structures.

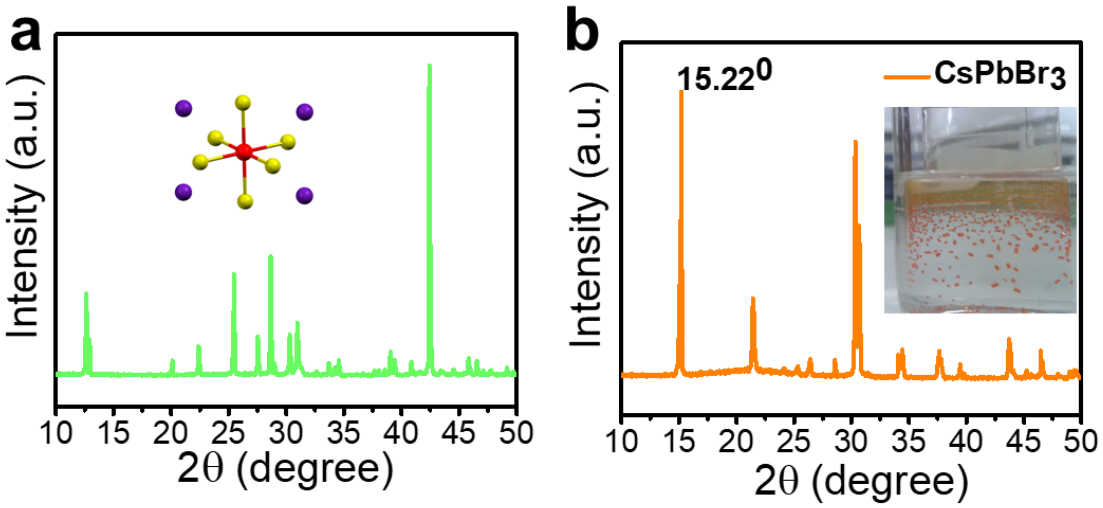

Figure S3. PXRD measurement. (a) PXRD of **2** SC. The PXRD pattern confirms the purity and trigonal structure of **2.** (b) PXRD pattern of $CsPbBr_3$. If $CsPbBr_3$ nanocrystals were trapped within bulk Cs_4PbBr_6, we should have observed the PXRD peak at 15.22° corresponding to (110) plane of $CsPbBr_3$. We have synthesized pure Cs_4PbBr_6 crystals for which no powder X-ray diffraction peaks corresponding to $CsPbBr_3$ are found. Thus, we exclude the possibility of $CsPbBr_3$ nanocrystals trapped within the bulk of Cs_4PbBr_6.

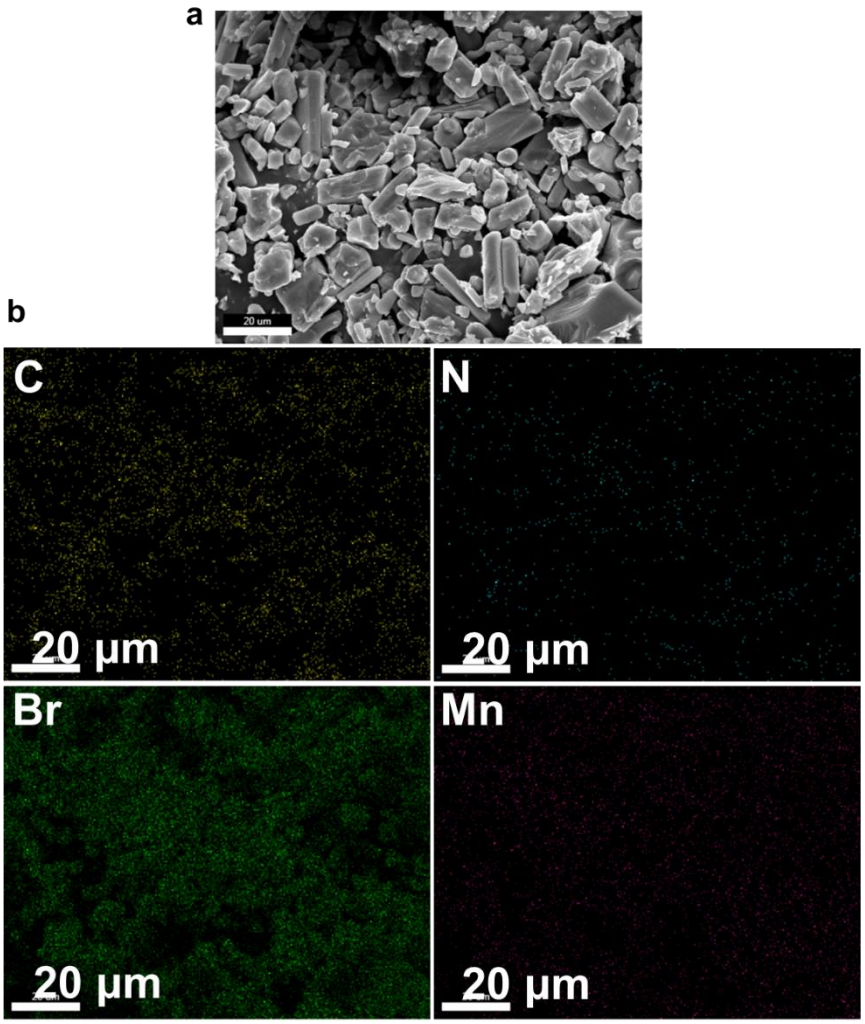

Figure S4. SEM-EDX. **a,** Morphology of (**1**) powder synthesized by SIP method **b,** SEM-elemental mapping. Presence of C, N, Mn and Br was confirmed from SEM-elemental mapping.

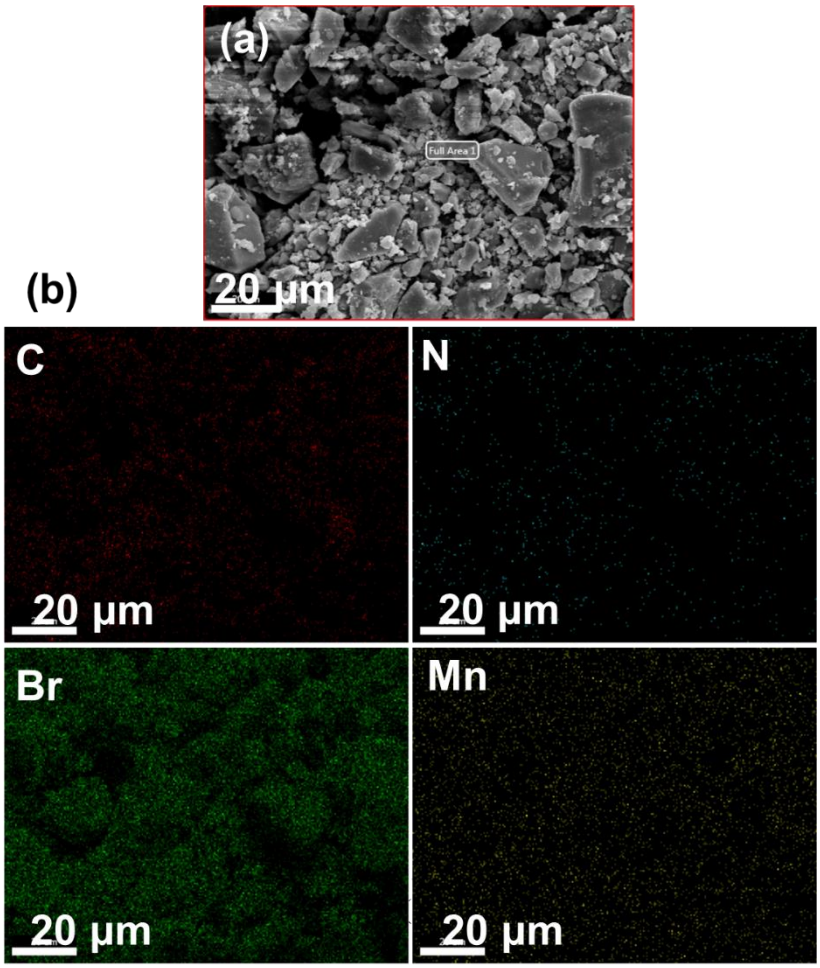

Figure S5. SEM-EDX elemental mapping. (a) Morphology of (**1)** SC (b) SEM-elemental mapping. Presence of C, N, Mn and Br was confirmed from SEM-elemental mapping.

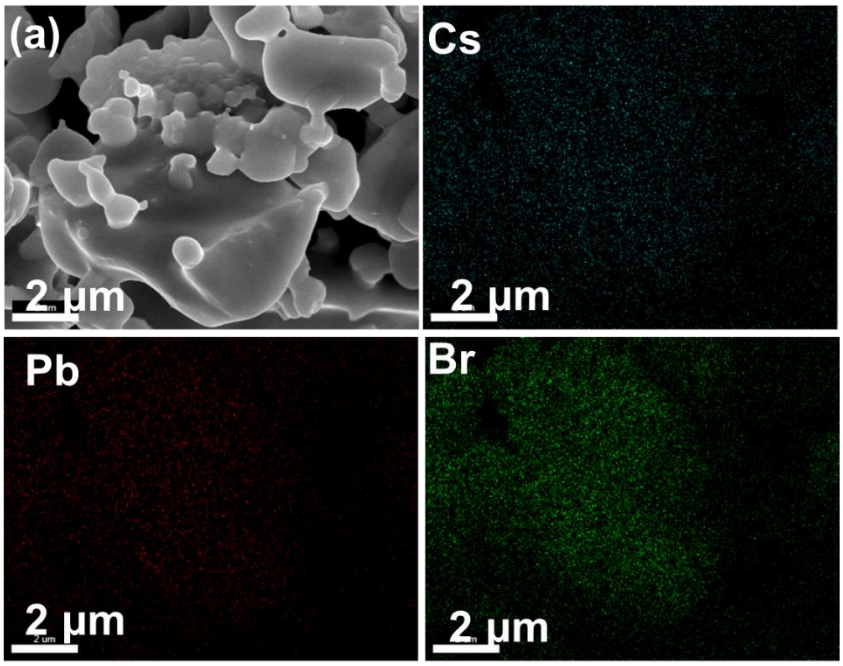

Figure S6. SEM-EDX elemental mapping. (a) Morphology of (**2**) SC (b) SEM-elemental mapping. Presence of Cs, Pb and Br was confirmed from SEM-elemental mapping.

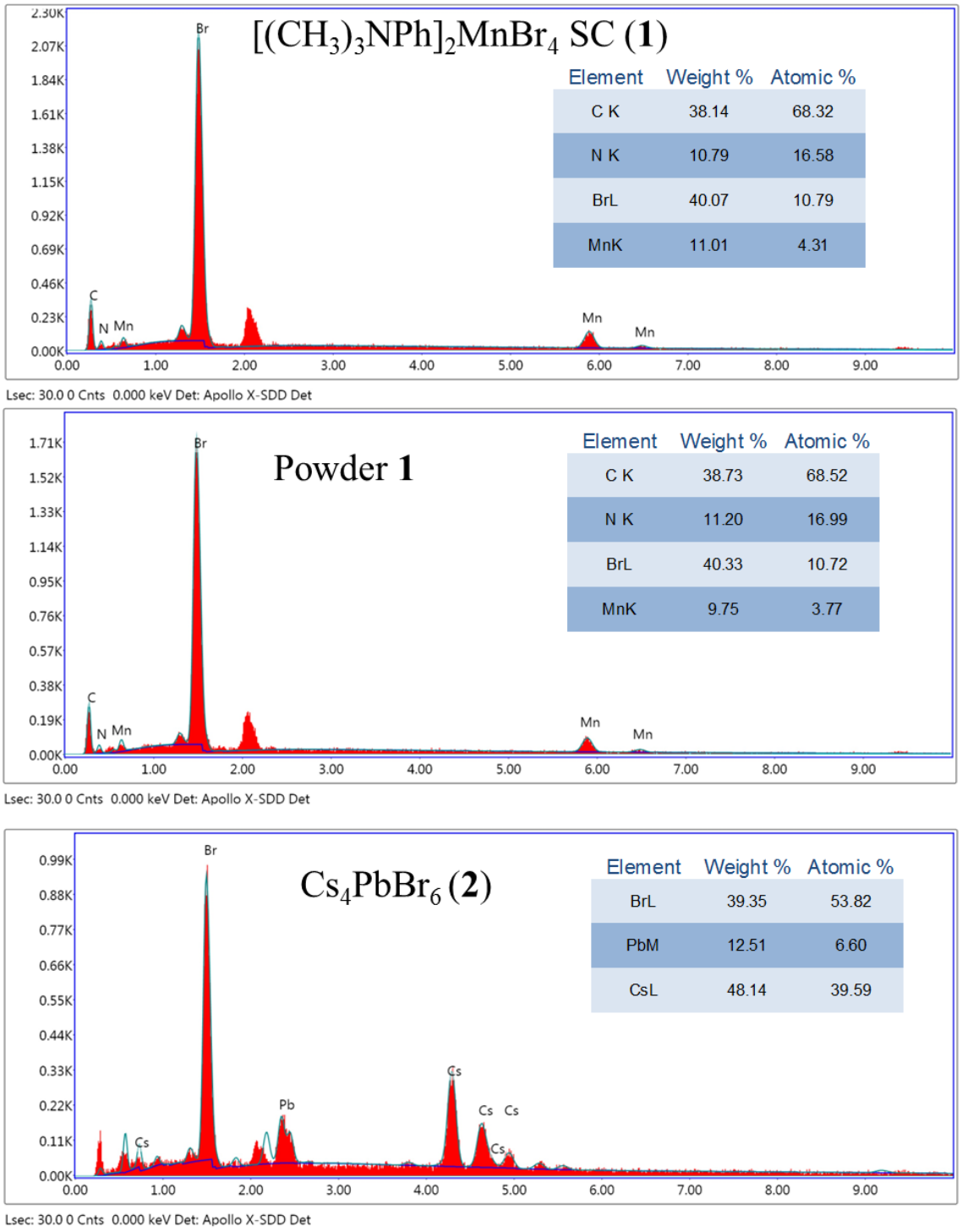

Figure S7. SEM-EDS. $[Me_3NPh]_2MnBr_4$ SC (**1**), powder (**1**) and Cs_4PbBr_6 (**2**)

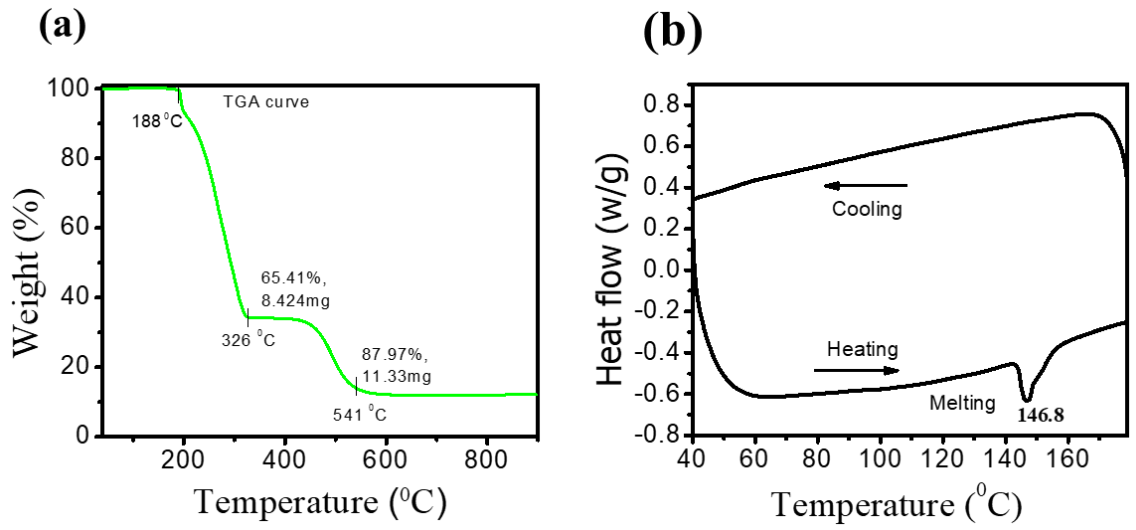

Figure S8. Thermo-gravimetric analysis (TGA) and differential scanning calorimetry (DSC) measurement. (a) Thermogravimetric analyses of **1** SC. Compound **1** was stable upto 188 ℃. (b) DSC measurements of **1** which melted at 146.8 ℃.

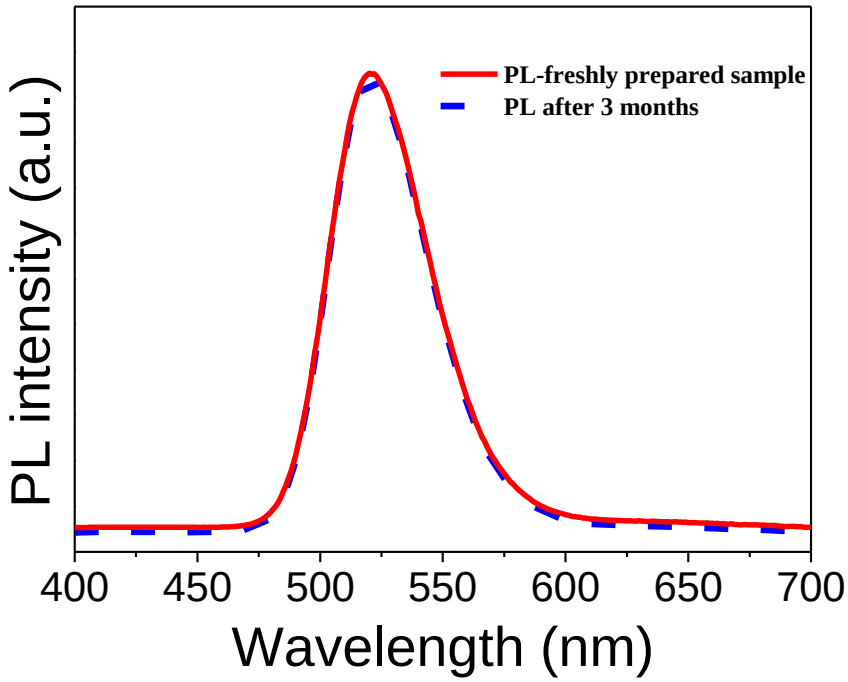

Figure S9. PL intensities of **1** before and after 3 months exposure in atmospheric environment

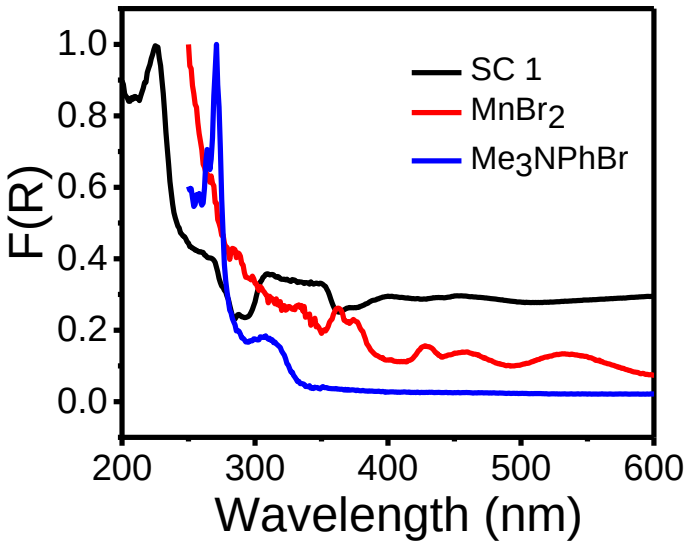

Figure S10. Kubelka-Munk plot. $MnBr_2$, Me_3NPhBr and $[Me_3NPh]_2MnBr_4$ (**1**) SC. F(R) is Kubelka-Munk function.

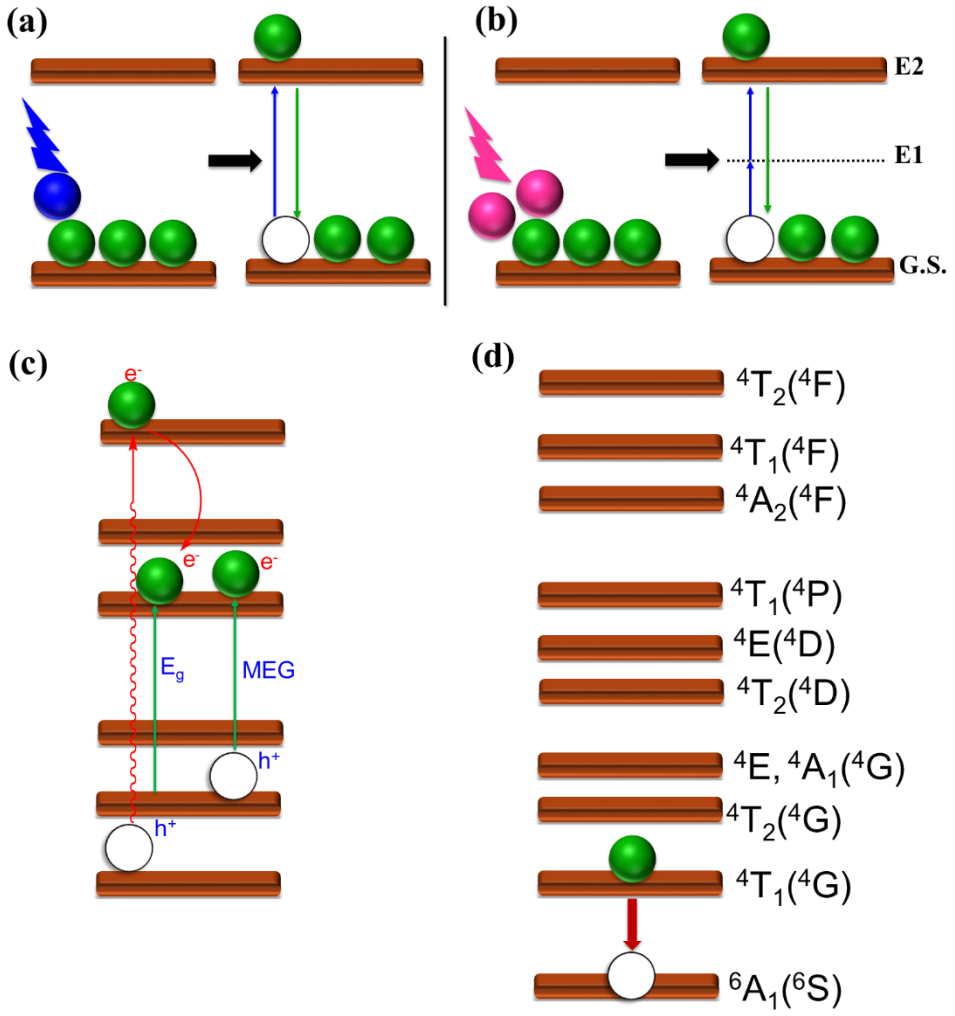

Figure S11. Schematic diagram for conventional absorption/luminescence, upconversion, and MEG. (a) one photon-one electron interaction (b) two photon-one electron interaction; Two low- energy incident photons excite one electron to the conduction band and high-energy photon is emitted when the electron comes back to ground state. E1 and E2 are the intermediate energy level and conduction band energy level, respectively, while G.S. is the ground state energy level. (c) Multiexciton generation (d) Tanabe-Sugano diagram for d^5 tetrahedral Mn(II) complex.

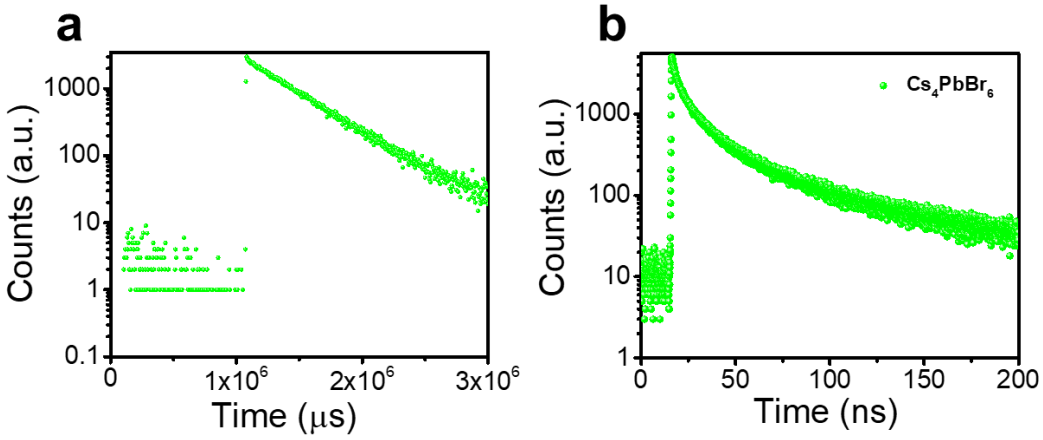

Figure S12. Life-time measurement. (a) Time resolved photoluminescence (TRPL) spectra of SC **1**. Excitation and emission wavelengths are 455 and 520 nm, respectively. The long decay channel indicates that SC **1** has long life-time which is as high as 400 μs. (b) TRPL decay curve for **2**. Average lifetime of **2** is 25 ns.

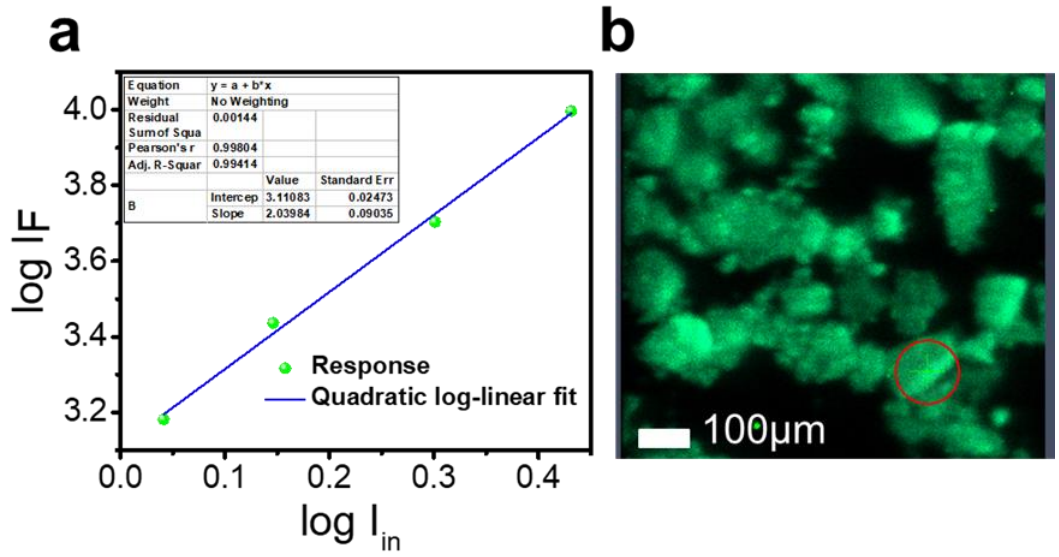

Figure S13. (a) Non-linear absorption induced PL in $[Me_3NPh]_2MnBr_4$ (**1**). The PL intensity depends non-linearly on excitation intensity. (b) Single particles image. The laser used for the study was 456 nm and the PL emission appeared at 520 nm.

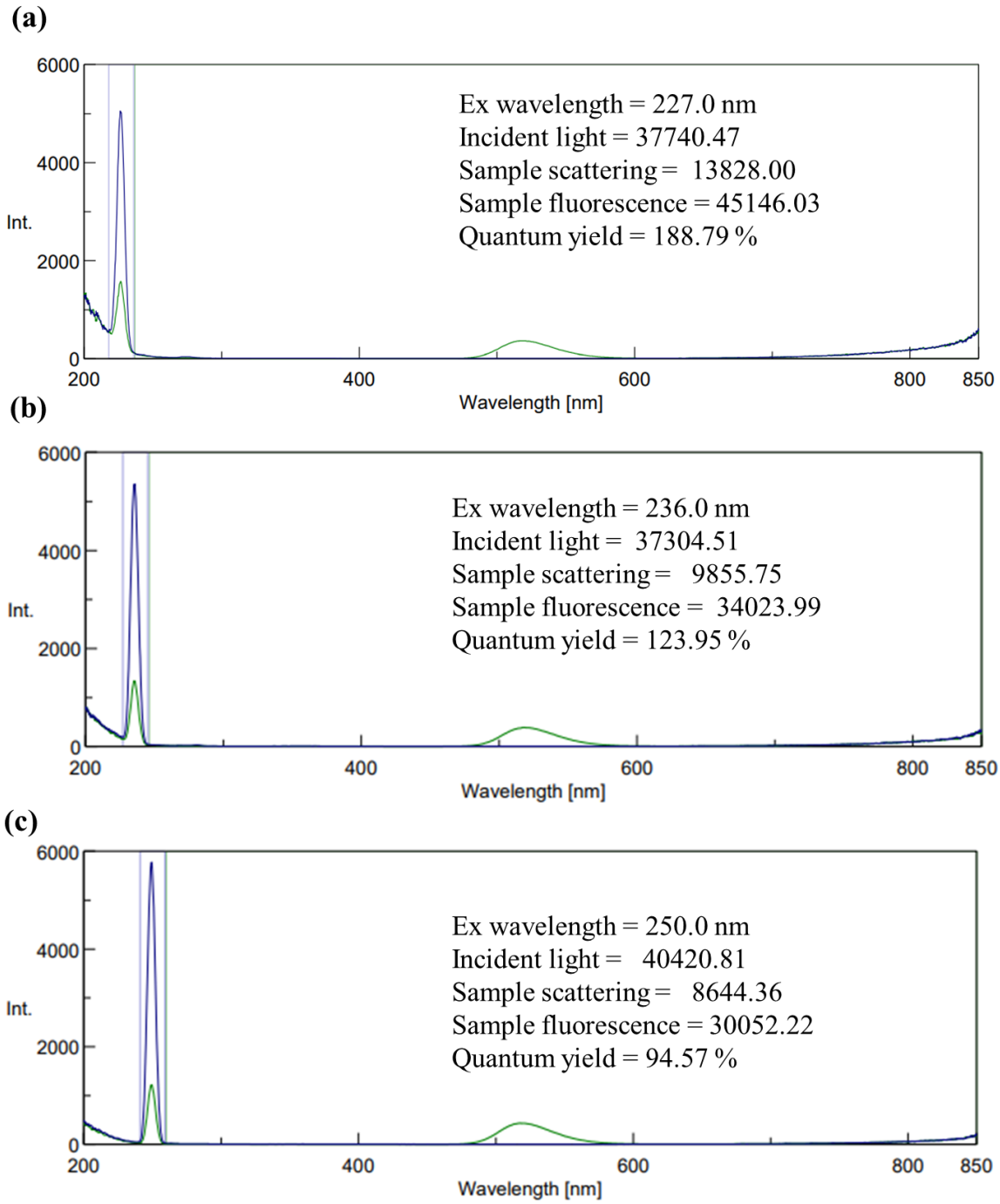

Figure S14. PL QY measurements of SCs of **1** at different excitation wavelengths: (a) 227 nm (b) 236 nm, and (c) 250 nm. Ex bandwidth = 5 nm, Em bandwidth = 5 nm, PMT voltage = 340 V, Scan speed = 1000 nm/min, Quantum yield [%] = $S_2/(S_0-S_1)$ ×100. S_1 = area scattered from the sample, S_2 = area emitted from sample, S_0 = area from incident light. S_0 was measured with nothing in the sample holder.

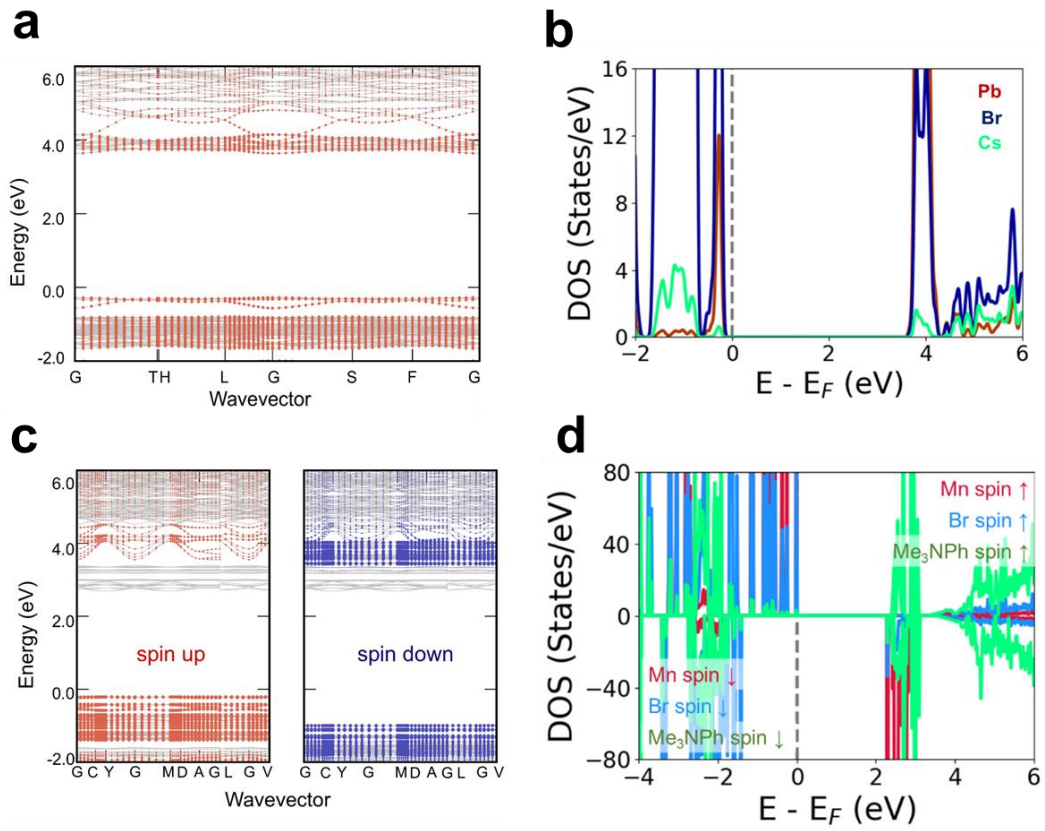

Figure S15. (a, b) The orbital projected electronic band structure (left) and projected density of states (right) of R$\bar{3}$c trigonal Cs_4PbBr_6 (**2**) at the PBE+TS level of theory. The red circle indicates the contribution of Pb and Br states. (c,d) The spin polarized orbital projected band structure (left) and Projected density of states (right) of **1** at the PBE+TS level of theory. Most of the spin up (red circle) and spin down (blue circle) of Mn and Br states in the valance and conduction bands form many discrete levels. Figure "d" which is already in Figure 4c in the main manuscript is redrawn here for comparison purpose with the Cs_4PbBr_6 case.

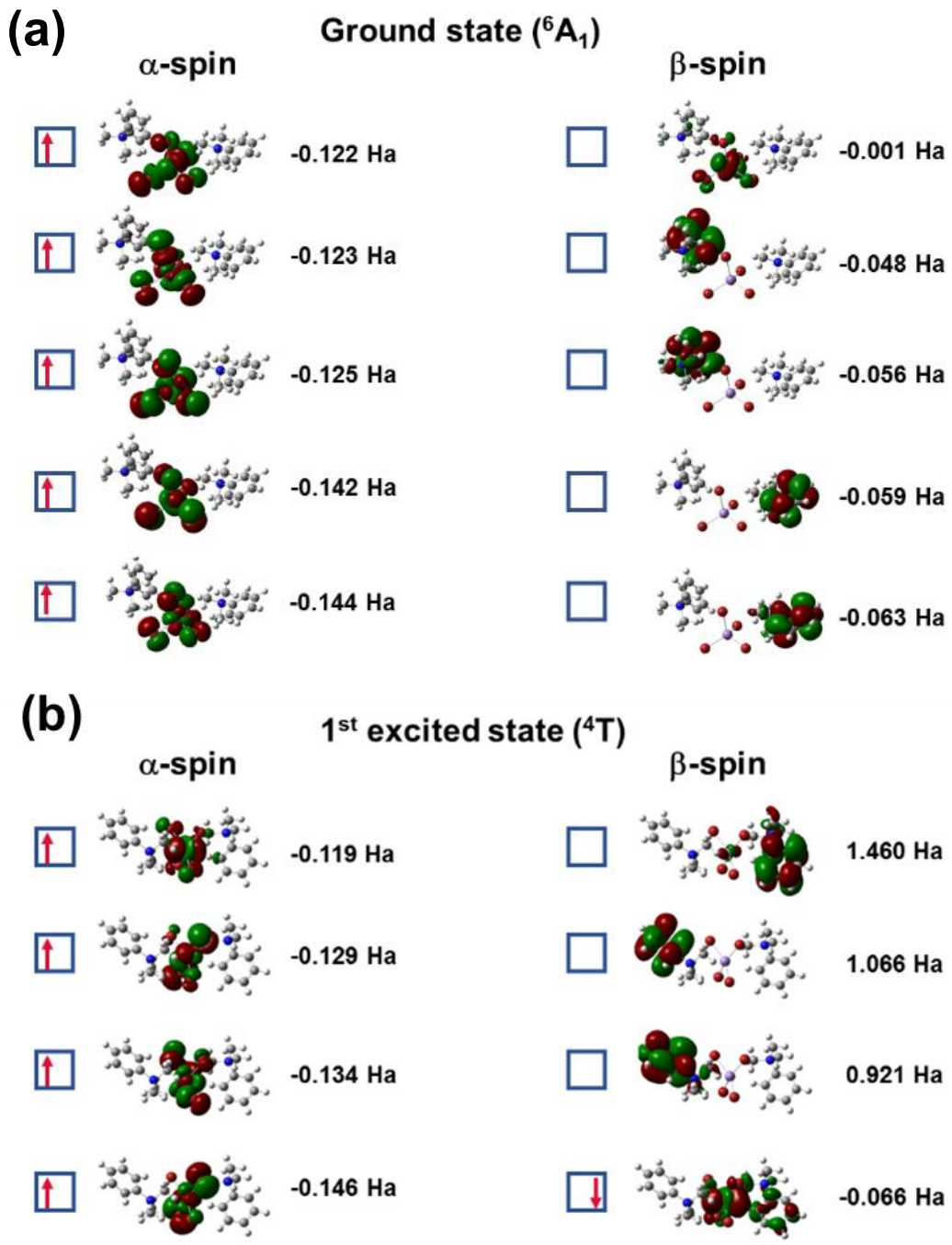

Figure S16. A molecular orbital energy level schematic of (a) the ground state $^6A_1$ and (b) the first excited state $^4A_1$ for $[Me_3NPh]_2MnBr_4$ unit at the PBE level of theory.

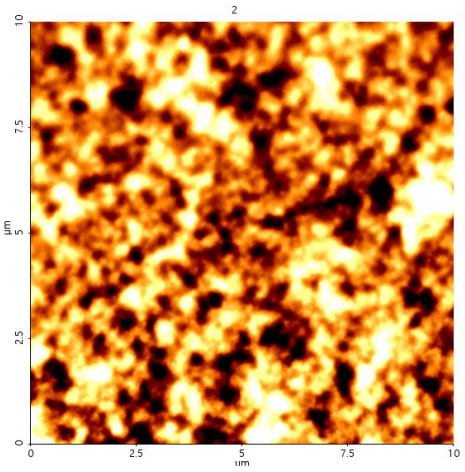

Figure S17. AFM images of mCP:TPBi:dopant **(1)** (13 wt%) film.

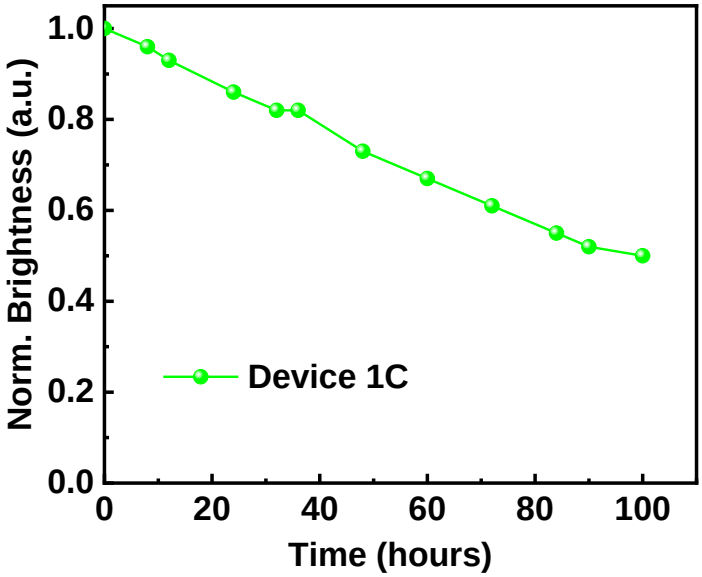

Figure S18. Lifetime of devices measured for Device 1C (with encapsulation).

References

1 M. Mittal, A. Jana, S. Sarkar, P. Mahadevan and S. Sapra, Size of the Organic Cation Tunes the Band Gap of Colloidal Organolead Bromide Perovskite Nanocrystals, *J. Phys. Chem. Lett.*, 2016, **7**, 3270–3277.

2 G. Kresse and J. Furthmüller, Efficiency of Ab-Initio Total Energy Calculations for

Metals and Semiconductors Using a Plane-Wave Basis Set, *Comput. Mater. Sci.*, 1996, **6**, 15–50.

3 A. Tkatchenko and M. Scheffler, Accurate Molecular Van Der Waals Interactions from Ground-State Electron Density and Free-Atom Reference Data, *Phys. Rev. Lett.*, 2009, **102**, 073005.

4 H. Yu, Y. Mei, Z. Wei, G. Mei and H. Cai, Fluorescent Properties of Manganese Halide Benzothiazole Inorganic–Organic Hybrids, *J. Fluoresc.*, 2016, **26**, 2295–2301.

5 C. Jiang, N. Zhong, C. Luo, H. Lin, Y. Zhang, H. Peng and C.-G. Duan, (Diisopropylammonium)$_2$MnBr$_4$: A Multifunctional Ferroelectric with Efficient Green-Emission and Excellent Gas Sensing Properties, *Chem. Commun.*, 2017, **53**, 5954–5957.

6 X.-W. Cai, Y.-Y. Zhao, H. Li, C.-P. Huang and Z. Zhou, Green-Light-Emitting Crystal Based on Organic-Inorganic Hybrid [($C_{10}H_{16}N$)]$_2$[$MnBr_4$] with High Emissive Quantum Yields and Large Crystal Size, *J. Mol. Struct.*, 2018, **1161**, 262–266.

7 L.-J. Xu, C.-Z. Sun, H. Xiao, Y. Wu and Z.-N. Chen, Green-Light-Emitting Diodes Based on Tetrabromide Manganese(II) Complex through Solution Process, *Adv. Mater.*, 2017, **29**, 1605739.

8 L.-K. Gong, Q.-Q. Hu, F.-Q. Huang, Z.-Z. Zhang, N.-N. Shen, B. Hu, Y. Song, Z.-P. Wang, K.-Z. Du and X.-Y. Huang, Efficient Modulation of Photoluminescence by Hydrogen Bonding Interactions between Inorganic [$MnBr_4$]$^{2-}$ Anions and Organic Cations, *Chem. Commun.*, 2019, **55**, 7303–7306.

9 M. Li, J. Zhou, M. S. Molokeev, X. Jiang, Z. Lin, J. Zhao and Z. Xia, Lead-Free Hybrid Metal Halides with a Green-Emissive [$MnBr_4$] Unit as a Selective Turn-On Fluorescent Sensor for Acetone, *Inorg. Chem.*, 2019, **58**, 13464–13470.

10 V. Morad, I. Cherniukh, L. Pöttschacher, Y. Shynkarenko, S. Yakunin and M. V. Kovalenko, Manganese(II) in Tetrahedral Halide Environment: Factors Governing Bright Green Luminescence, *Chem. Mater.*, 2019, **31**, 10161–10169.

11 L. Mao, P. Guo, S. Wang, A. K. Cheetham and R. Seshadri, Design Principles for Enhancing Photoluminescence Quantum Yield in Hybrid Manganese Bromides, *J. Am. Chem. Soc.*, 2020, **142**, 13582–13589.

12 L.-J. Xu, X. Lin, Q. He, M. Worku and B. Ma, Highly Efficient Eco-Friendly X-Ray Scintillators Based on an Organic Manganese Halide, *Nat. Commun.*, 2020, **11**, 4329.

13 A. Jana, V. G. Sree, Q. Ba, S. C. Cho, S. U. Lee, S. Cho, Y. Jo, A. Meena, H. Kim and H. Im, Efficient Organic Manganese (ii) Bromide Green-Light-Emitting Diodes Enabled by Manipulating the Hole and Electron Transport Layer, *J. Mater. Chem. C*, 2021, **9**, 11314–11323.

14 A. Jana, S. Zhumagali, Q. Ba, A. S. Nissimagoudar and K. S. Kim, Direct Emission from Quartet Excited States Triggered by Upconversion Phenomena in Solid-Phase Synthesized Fluorescent Lead-Free Organic–Inorganic Hybrid Compounds, *J. Mater. Chem. A*, 2019, **7**, 26504–26512.

15 C. Jiang, H. Fu, Y. Han, D. Li, H. Lin, B. Li, X. Meng, H. Peng and J. Chu, Tuning the Crystal Structure and Luminescence of Pyrrolidinium Manganese Halides via Halide Ions, *Cryst. Res. Technol.*, 2019, **54**, 1800236.

16 G. Hu, B. Xu, A. Wang, Y. Guo, J. Wu, F. Muhammad, W. Meng, C. Wang, S. Sui, Y. Liu, Y. Li, Y. Zhang, Y. Zhou and Z. Deng, Stable and Bright Pyridine Manganese Halides for Efficient White Light-Emitting Diodes, *Adv. Funct. Mater.*, 2021, **31**, 2011191.